


Imaging Stacking-Dependent Surface Plasmon Polaritons in Trilayer Graphene

Yilong Luan,^{1,2} Jun Qian,^{1,3} Minsung Kim,^{1,2} Kai-Ming Ho,^{1,2} Yi Shi,³ Yun Li,³ Cai-Zhuang Wang,^{1,2} Michael C. Tringides,^{1,2} and Zhe Fei^{1,2,*}

¹*Department of Physics and Astronomy, Iowa State University, Ames, Iowa 50011, USA*

²*Ames Laboratory, U.S. Department of Energy, Iowa State University, Ames, Iowa 50011, USA*

³*National Laboratory of Solid-State Microstructures, School of Electronic Science and Engineering, Collaborative Innovation Center of Advanced Microstructures, Nanjing University, Nanjing 210093, People's Republic of China*

 (Received 23 March 2022; revised 29 May 2022; accepted 5 July 2022; published 18 August 2022)

We report an infrared (IR) imaging study of trilayer graphene (TLG) with both ABA (Bernal) and ABC (rhombohedral) stacking orders using the scattering-type scanning near-field optical microscope (SSNOM). With the SSNOM operating in the mid-IR region, we map in real space the surface plasmon polaritons of ABA TLG and ABC TLG, which are tunable with electrical gating. Through quantitative modeling of plasmonic imaging data, we find that the plasmon wavelength of ABA TLG is significantly larger than that of ABC TLG, resulting in a sizable impedance mismatch and hence a strong plasmon reflection at the ABA/ABC lateral junction. Further analysis indicates that the different plasmonic responses of the two types of TLG are directly linked to their distinct electronic structures and carrier properties. Our work uncovers the physics behind the stacking-dependent plasmonic responses of TLG and sheds light on future applications of TLG and the ABA/ABC junctions in IR plasmonics and planar nano-optics.

DOI: [10.1103/PhysRevApplied.18.024052](https://doi.org/10.1103/PhysRevApplied.18.024052)

I. INTRODUCTION

In recent years, graphene plasmonics has become an active research field due to the discovery of surface plasmon polaritons (SPPs) in single-layer graphene (SLG) with many superior properties, such as high confinement, gate tunability, and a broad spectral range from terahertz (THz) to infrared (IR) [1–18]. Moreover, graphene can serve as a basic building block for the construction of a family of plasmonic materials by van der Waals stacking. For example, it is found that AB-stacking bilayer graphene (BLG) supports gate-tunable IR SPPs [19], which can couple strongly with the intrinsic phonons of BLG [20] and exhibit peculiar reflection properties at the AB/BA domain walls [21]. Plasmonic studies are also performed on twisted BLG, where SPPs are demonstrated to have a sensitive dependence on the twist angle between the two graphene layers [22]. So far, experimental plasmonic studies are focused mainly on SLG and BLG. The plasmonic responses of multilayer graphene (MLG) with thicknesses beyond two layers are not fully explored.

One of the most popular MLGs is trilayer graphene (TLG), which is formed by stacking three graphene layers together. TLG exfoliated from natural graphite has two common stacking orders: ABA (Bernal) stacking and ABC

(rhombohedral) stacking [see insets of Figs. 1(b) and 1(c)]. The two stacking orders of TLG result in their dramatically different electronic structures. In Figs. 1(b) and 1(c), we plot the band structures of both ABA-stacked TLG (ABA TLG) and ABC-stacked TLG (ABC TLG) calculated with the tight-binding method [23,24]. Details of the calculations are given in Appendix F. The band structure of ABA TLG [Fig. 1(b)] close to the charge-neutrality point consists of a set of Dirac bands (labeled as “ $\nu 1$ ”) like those of single-layer graphene and a set of parabolic bands (labeled as “ $\nu 2$ ”) like those of AB-stacked BLG. Therefore, the low-energy carriers in ABA TLG are a mixture of massless and massive carriers. The ABC TLG [Fig. 1(c)], on the other hand, has a set of parabolic bands (labeled as “ $\nu 3$ ”) at low energies, so the carriers of ABC TLG are massive. TLG is studied extensively by transport, Raman, and far-field optical spectroscopies, where distinct electronic and phononic responses are observed in the two types of stacking orders [25–33]. Recently, near-field imaging and spectroscopy have also been used to map in real space the stacking structures, domain walls, and hot-electron phonons of TLG with high spatial resolution [34–39].

Here, we perform a systematic nano-IR imaging study on TLG to explore the stacking-dependent plasmonic responses. To image SPPs in TLG, we employ a scattering-type scanning near-field optical microscope (SSNOM) operating in the mid-IR region. The SSNOM is built based

*zfei@iastate.edu

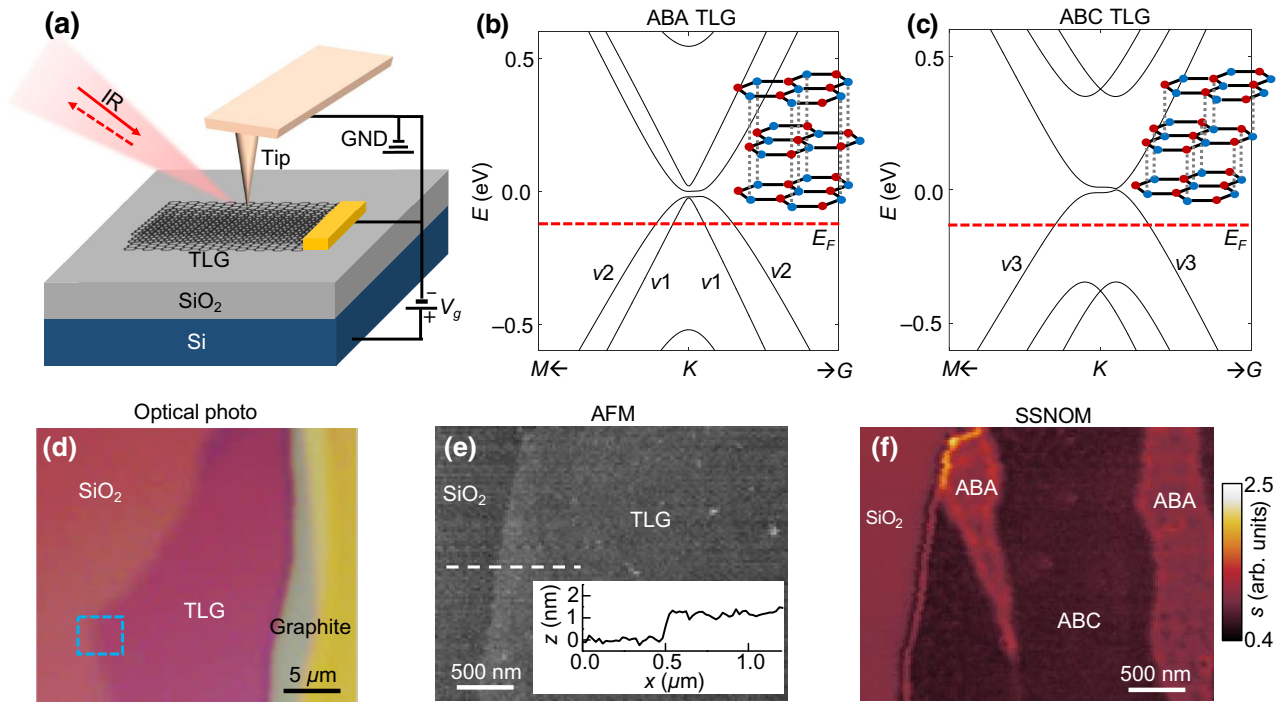


FIG. 1. (a) Illustration of the nano-IR imaging experiment of TLG with SSNOM. GND, ground. (b),(c) Band structures and lattice structures (insets) of ABA TLG and ABC TLG, respectively. Here, $v1$, $v2$, and $v3$ mark the three sets of bands that are responsible for the plasmonic responses of the two types of TLG. (d) Optical photograph of a TLG sample on a SiO_2/Si substrate. (e),(f) AFM and nano-IR imaging data over the sample region marked in panel (d) (blue rectangle). Inset of panel (e) plots the AFM topography profile taken along the white dashed line.

on an atomic force microscope (AFM), so we can obtain simultaneously the nano-IR and AFM topography images. For IR excitations, we utilize a continuous-wave (cw) CO_2 laser with a wavelength set to $11.2 \mu\text{m}$, corresponding to a photon energy of 0.11 eV . Upon laser illumination, the metalized tip of the SSNOM can efficiently launch and detect SPPs [14,15]. The samples studied here are obtained by the mechanical exfoliation of bulk graphite crystals onto standard SiO_2/Si substrates. A more detailed introduction to the experimental setup is given in Appendix A.

II. RESULTS AND DISCUSSION

In Fig. 1(d), we show an optical photograph of a typical sample region that includes both ABA TLG and ABC TLG. We determine the thickness and stacking orders of these samples by a combination of AFM and nano-IR imaging and spectroscopy via SSNOM. With AFM, we measure the thickness of the sample to be about $1.0\text{--}1.2 \text{ nm}$ uniformly throughout the sample [see Fig. 1(e) and inset]. With nano-IR imaging [Fig. 1(f)], we can visualize the two stacking orders: ABA TLG has a higher IR signal compared to that of ABC TLG, as discussed in detail in the literature [35,36]. Here, the signal shown in the SSNOM images corresponds to the near-field scattering amplitude

(s) [14,15]. In all the SSNOM images and spectra, s is normalized to that of the SiO_2/Si substrate. With nano-IR spectroscopy, we are able to measure the IR phonon resonance [39], which can also be used to distinguish between the two stacking orders: ABC TLG has a strong IR phonon resonance, while ABA TLG's IR phonon is too weak to be seen (see Appendix B).

A. Nano-IR imaging of SPPs in TLG

From Fig. 1(f), we can see bright fringes close to the edges of the TLG sample. To visualize more clearly these fringes, we plot in Fig. 2 magnified nano-IR images close to the sample edge taken at various back-gate voltages. Here, the voltages correspond to $V_g - V_{\text{CN}}$, where V_g is the applied gate voltage and V_{CN} corresponds to the charge-neutrality point ($V_g - V_{\text{CN}} < 0$ corresponds to hole doping). As shown in Fig. 2, we can see bright fringes close to the edges of both ABA TLG and ABC TLG, which are generated due to the interference between tip-launched and edge-reflected SPPs [14,15,19,21]. These plasmonic fringes are stronger at higher doping (i.e., larger $|V_g - V_{\text{CN}}|$) and almost completely disappear close to the charge-neutrality point (i.e., $V_g - V_{\text{CN}} = 0 \text{ V}$). Such gate dependence is signature behavior of SPPs in graphene or other two-dimensional (2D) materials. Moreover, we find that the

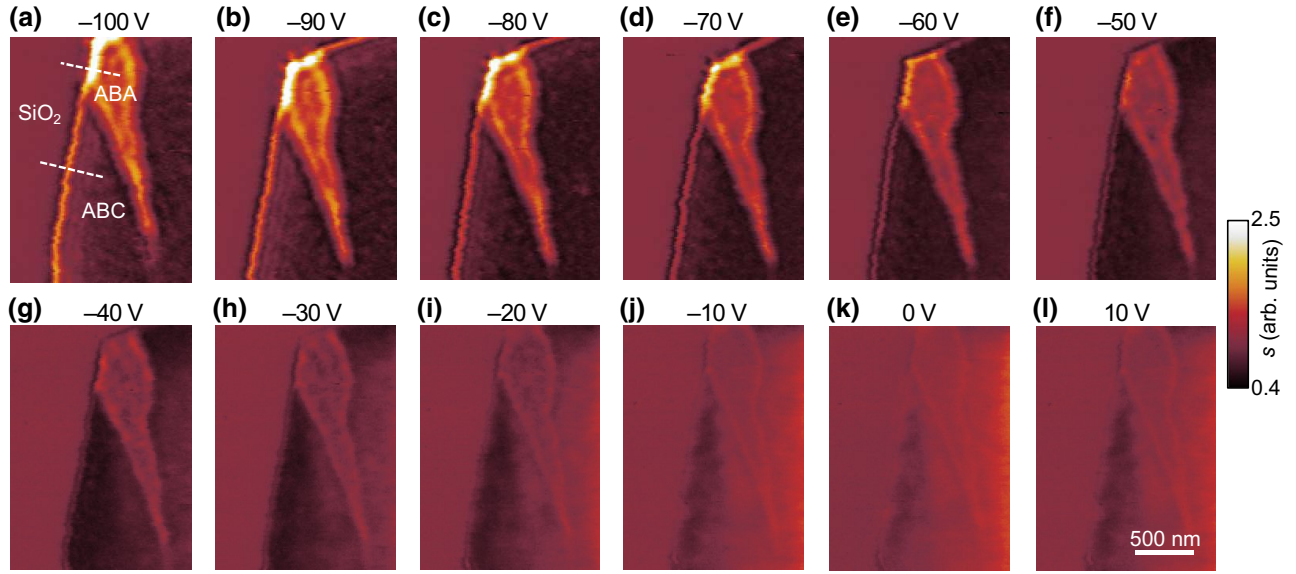


FIG. 2. Nano-IR imaging data of ABA TLG and ABC TLG at various gate voltages. Voltages marked here correspond to $V_g - V_{CN}$. Dashed lines in panel (a) mark the directions along which we extract the line profiles shown in Fig. 3.

fringes are different in the two types of TLG: plasmonic fringes are stronger and brighter in ABA TLG than those of ABC TLG.

B. Numerical modeling of the plasmonic fringe profiles

For quantitative analysis, we extract the line profiles perpendicular to the edges of ABA TLG and ABC TLG along the white dashed lines in Fig. 2(a). A selected set of line profiles (black curves) at different gate voltages are plotted in Fig. 3. Here, the peaks in the profiles correspond to the bright fringes in the nano-IR images in Fig. 2. To extract the key plasmonic parameters of TLG, we fit the line profiles with a quantitative model that is introduced in detail in previous works [14,19,22]. The key modeling parameter of the sample is the plasmonic wavevector, q_p , based on which we can obtain the plasmon wavelength, $\lambda_p \equiv 2\pi/\text{Re}(q_p)$, and plasmon-damping rate, $\gamma_p \equiv \text{Im}(q_p)/\text{Re}(q_p)$. The modeling profiles are plotted as red dashed profiles in Fig. 3, which show good agreement with the experimental profiles. From the fitting, we determine λ_p and γ_p of both ABA TLG and ABC TLG, which are plotted in Fig. 4(a) and Fig. 8 in Appendix E, respectively. We discuss mainly λ_p of TLG in the main text and the discussions of γ_p can be found in Appendix E. As shown in Fig. 4(a), λ_p increases systematically with $|V_g - V_{CN}|$ for both ABA TLG and ABC TLG. This is expected since higher doping leads to higher conductivity, and hence, a larger λ_p . Moreover, we find that λ_p of ABA TLG is much larger than that of ABC TLG, which is the key origin for the distinct plasmonic and nano-IR responses of the two types of TLG [see Figs. 1(f) and 2].

C. Theoretical calculations of SPPs in TLG

The plasmon wavelength λ_p is directly associated with the optical conductivity, $\sigma(\omega)$, of the sample. Under the long-wavelength and 2D approximation, the plasmon wavevector (q_p) can be written as [14]

$$q_p \approx ik\omega/2\pi\sigma(\omega). \quad (1)$$

Here, $\kappa \approx (\epsilon_S + 1)/2$ is the effective dielectric constant of the environment, and ϵ_S is the permittivity of SiO_2 . Under the Drude approximation, $\sigma(\omega)$ can be written as $\sigma(\omega) = \sigma_0/(1 - i\omega\tau)$, where σ_0 is the dc conductivity and τ is the carrier relaxation time. Therefore, the plasmon wavelength, $\lambda_p \equiv 2\pi/\text{Re}(q_p)$, is roughly proportional to σ_0 . Based on the Einstein relation, σ_0 has the following form:

$$\sigma_0 \approx \sum_{\text{all bands}} \frac{1}{2} e^2 N(E_F) v_F(E_F)^2 \tau. \quad (2)$$

In Eq. (2), $N(E_F)$ is the carrier density at the Fermi energy (E_F) and v_F is the Fermi velocity. The summation is over all bands crossing the Fermi level [see Figs. 1(b) and 1(c)]. Based on Eqs. (1) and (2), we know that the plasmon wavelength, λ_p , is roughly proportional to the DOS and v_F^2 at E_F .

To determine DOS and v_F^2 at the Fermi level, we first calculate E_F at various gate voltages. As shown in Fig. 4(b), the E_F of ABA TLG is close to and slightly higher than that of ABC TLG throughout the voltage region. We then calculate the total DOS and v_F^2 at the Fermi level for both types of TLG, which are plotted in Figs. 4(c) and 4(d), respectively. From Fig. 4(c), one can see that the

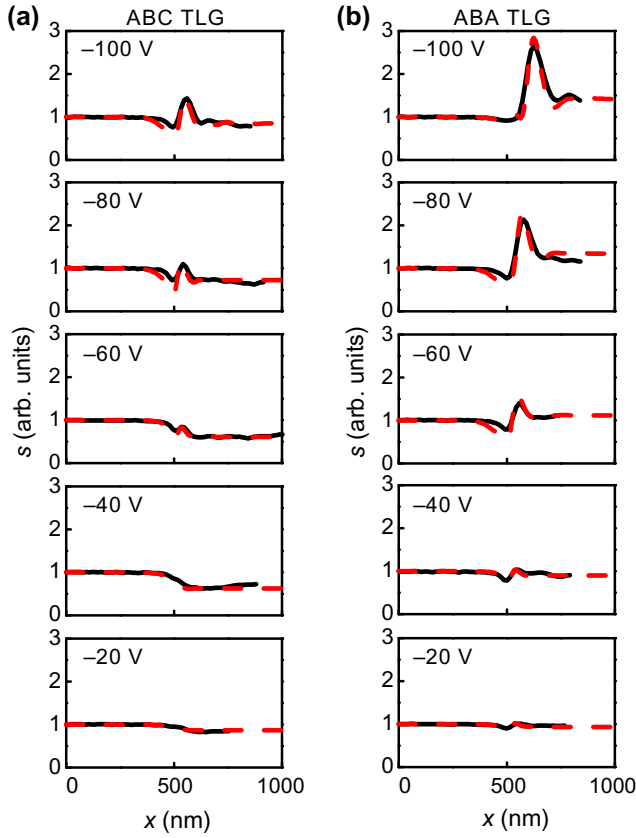


FIG. 3. Plasmon fringe profiles of ABC TLG and ABA TLG at various gate voltages ($V_g - V_{CN}$). Black curves are experimental line profiles taken perpendicular to sample edges (along white dashed lines) of the nano-IR images in Fig. 2. Red curves are the fitting profiles using a quantitative SSNOM model.

total DOS of ABA TLG is slightly larger ($\leq 20\%$) than that of ABC TLG in the high-doping regime ($|V_g - V_{CN}| > 40$ V) and smaller at lower doping. A more dramatic difference can be seen in Fig. 4(d), where v_F^2 of the Dirac-like bands of ABA TLG [band $\nu 1$, see Fig. 1(b)] is significantly larger than that of the parabolic bands [band $\nu 2$ of ABA TLG and $\nu 3$ of ABC TLG, see Figs. 1(b) and 1(c)]. In the high-doping regime, v_F^2 of the Dirac bands is about 2 times that of the parabolic bands. The ratio increases to over 10 times at lower doping, as the parabolic bands become more flattened. Based on Figs. 1(b) and 1(c), we believe that the big deviation of λ_p in ABA TLG and ABC TLG shown in our data is mainly due to the difference in Fermi velocity. In other words, the Dirac carriers of ABA TLG with higher v_F are mainly responsible for the higher conductivity and larger λ_p of ABA TLG.

By calculating DOS and v_F^2 for every single band involved, we are able to compute λ_p of ABA TLG and ABC TLG using Eqs. (1) and (2) (Einstein relation), which are plotted in Fig. 4(a) as dashed curves. Calculations are also performed using the optical conductivity computed with the Kubo formula [solid curves in Fig. 4(a)] (see

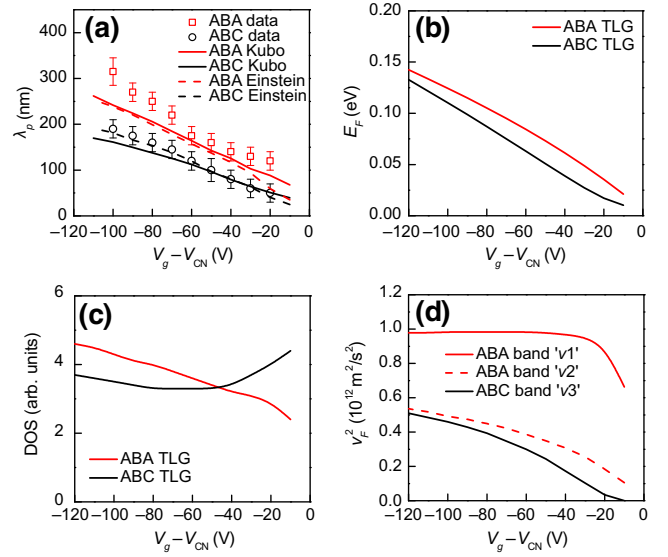


FIG. 4. (a) Experimental (data points) and theoretical (curves) plasmon wavelength, λ_p , of ABA TLG and ABC TLG at various gate voltages ($V_g - V_{CN}$). (b) Calculated E_F at various gate voltages for both ABA TLG and ABC TLG. (c) Calculated DOS at various gate voltages for both ABA TLG and ABC TLG. (d) Calculated v_F^2 at various gate voltages for the Dirac-like bands $\nu 1$ and parabolic-like bands $\nu 2$ of ABA TLG [see Fig. 1(b)] and for the parabolic bands $\nu 3$ of ABC TLG [see Fig. 1(c)].

Appendix F for details of the calculations). The results of the two theoretical methods agree with each other. From Fig. 4(a), one can see that both the doping and stacking dependence of the theoretical curves are qualitatively consistent with experimental data points. We also notice that the calculated λ_p of ABA TLG is smaller ($\leq 30\%$) than the experimental data points in the high-doping regime. The causes of the deviation are not fully understood. It could be due to the tight-binding parameters (see Appendix F) that we adopt from previous reports in the literature [32,40], which might not be perfect for our TLG samples.

D. Plasmonic responses of the ABA/ABC junctions

Finally, we wish to discuss the plasmonic responses at planar junctions of ABA TLG and ABC TLG (termed “domain-wall solitons” in Refs. [34,41]). As shown in Figs. 1 and 2, bright plasmon fringes can also be seen at the ABA/ABC junctions, indicating that they are efficient plasmonic reflectors. This is primarily due to the big difference in λ_p of the two types of TLG, leading to a sizable impedance mismatch of SPPs. Potential applications of these junctions include plasmonic resonators, where SPPs can be strongly confined and resonantly enhanced. One simple example is demonstrated in Figs. 5(a)–5(c), where a

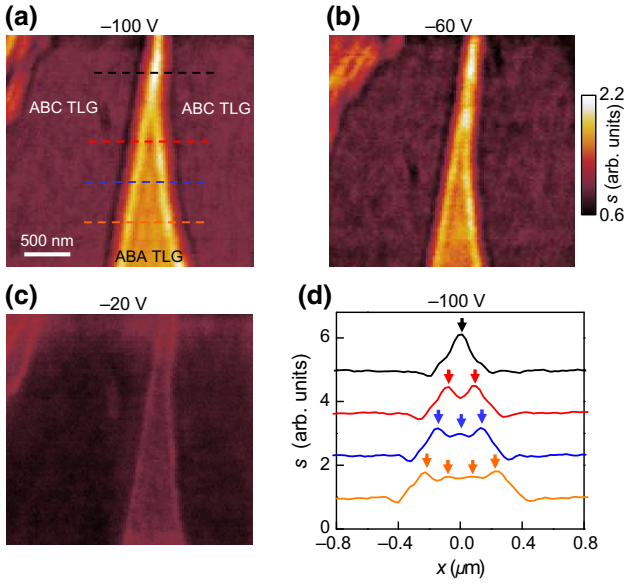


FIG. 5. (a)–(c) Nano-IR imaging data of a sample area containing an ABC/ABA/ABC TLG junction at various gate voltages ($V_g - V_{CN}$). (d) Line profiles extracted along the dashed lines in panel (a). Arrows mark the resonant peaks in the profiles.

special plasmon resonator formed by two ABA/ABC junctions is shown. Due to plasmon reflection at the two junctions, one can see the plasmon fringe pattern evolves systematically with gate voltages and the width of ABA TLG. At $V_g - V_{CN} = -100$ V [see Fig. 5(a) and the fringe profiles in Fig. 5(d)], the number of plasmon fringes or peaks drops as the two junctions get closer to each other. Resonant enhancement is observed when the width of ABA TLG drops to about 300 nm, where one strong plasmon fringe or peak is observed [see the black profile in Fig. 5(d)]. Similar plasmonic patterns have been studied previously in etched graphene nanoribbons with the graphene edges as the plasmonic reflectors [15]. These graphene edges potentially have a lot of dangling bonds, so they are sensitive to chemical dopants and air molecules under ambient conditions. The ABA/ABC junctions of TLG, on the other hand, preserve relatively intact crystal structures [35,42], so they are more robust and less sensitive to the environment. Moreover, it is demonstrated that these junctions can be engineered in a controllable way by a variety of physical or chemical methods [35,36,38,41–44]. Therefore, plasmonic resonators based on ABA/ABC planar junctions are, in principle, reconfigurable, which is not possible for those fabricated with lithography patterning and etching.

III. CONCLUSION

We perform a systematic nano-IR imaging study of SPPs in TLG with both ABA and ABC stacking orders. Through quantitative modeling of the interference fringe profiles of SPPs, we find that the plasmon wavelength

of ABA TLG is significantly higher than that of ABC TLG, which is mainly due to the larger Fermi velocity of Dirac carriers in ABA TLG. Furthermore, we find that the planar junctions of ABA TLG and ABC TLG are efficient plasmonic reflectors. Plasmonic resonators formed by these junctions enable nanoscale localization and resonant enhancement of SPPs. Our work paves the way for future applications of the two types TLG and their planar junctions in reconfigurable IR plasmonics and nano-optics.

ACKNOWLEDGMENTS

This work is supported by the U.S. Department of Energy (DOE), Office of Science, Basic Energy Sciences, Materials Science and Engineering Division. The research is performed at Ames Laboratory, which is operated for the U.S. DOE by Iowa State University under Contract No. DE-AC02-07CH11358. J.Q. and Y.L. are supported by the Natural Science Foundation of Jiangsu Province (Grant No. BK20211507), the National Natural Science Foundation of China (Grants No. 51861145202 and No. 61861166001), and the National Key Research and Development Program of China (Grant No. 2021YFA0715600).

APPENDIX A: EXPERIMENTAL SETUP

To perform nano-IR imaging studies of SPPs in TLG, we employ a SSNOM from Neaspec GmbH. The SSNOM is built based on the tapping-mode AFM. The tapping frequency is about 270 kHz, and the tapping amplitude is set to be around 50 nm. The AFM tips used in the work are Pt/Ir-coated silicon tips (NanoAndMore GmbH). The radius of the tip apex is about 25 nm, which defines the spatial resolution of the SSNOM. The excitation laser used in this work is a mid-IR CO₂ laser (Access Laser Co.) with a wavelength tunable from 10.7 to 11.3 μm . Throughout this work, we set the laser wavelength to be 11.2 μm . Upon laser excitation, the tip acts as both the launcher and scatterer of SPPs. The experimental observable of the SSNOM is the complex scattering signal demodulated at the n th ($n = 3$ in the current work) harmonic of the tapping frequency. We discuss mainly the amplitude part of the signal, which is sufficient for the description of the plasmonic responses.

APPENDIX B: SAMPLE FABRICATION AND CHARACTERIZATION

Our samples are prepared by the mechanical exfoliation of bulk graphite and then transferred to the Si wafer coating with a 285-nm-thick SiO₂ layer. Back gating is used to tune the carrier density of the samples. As discussed in the main text, we use AFM to determine the sample thickness and use nano-IR imaging or spectroscopy to distinguish ABA TLG and ABC TLG. As shown in Fig. 1(f), ABA TLG and ABC TLG are easily distinguishable due to the clear IR

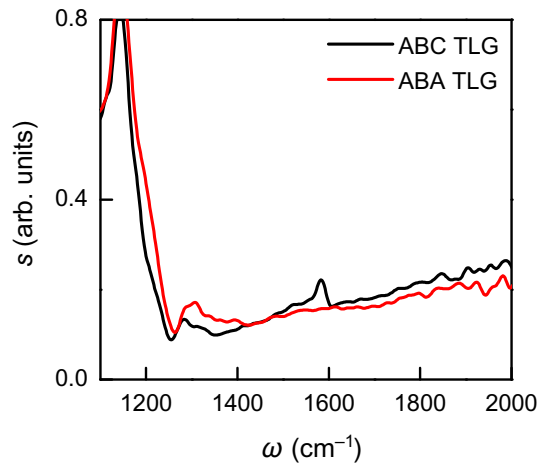


FIG. 6. Nano-IR spectra of both ABA TLG and ABC TLG samples from Fig. 1(d).

contrast originating from their different optical conductivities. Besides nano-IR imaging, we also record the nano-IR spectra of the two types of TLG. In Fig. 6, we plot the nano-IR spectra of both ABA TLG and ABC TLG, where one can see that the spectrum (black curve) of ABC TLG has a clear IR phonon resonance close to 1600 cm^{-1} . In the case of the spectrum (red curve) of ABA TLG, there is no clear strong phonon resonance. More discussions of the distinct phonon responses of ABA TLG and ABC TLG are given in the previous work [39].

APPENDIX C: FRINGE-FORMATION MECHANISM

In Figs. (1) and (2), we show the near-field-amplitude images of TLG, where we can see bright fringes close to the edges of the samples. These fringes are generated due to plasmonic interference close to the sample edges, boundaries, or defects, where SPPs can be effectively reflected. The general mechanism for the interference is sketched in Fig. 7. When excited by the IR laser, the SSNOM tip launches SPPs. These SPPs propagate toward the sample edge and then get reflected back to the tip.

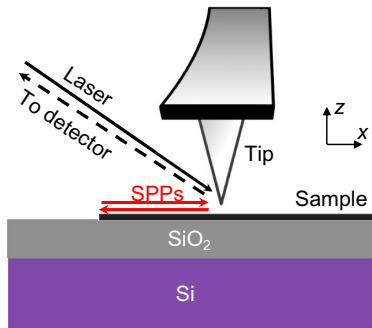


FIG. 7. Illustration of the interference mechanism of SPPs.

The reflected SPPs then interfere with those just generated by the tip. Depending on the distance between the tip and sample edge, the interference can be constructive or destructive. In the case of constructive interference, the E_z field underneath the tip will be strongly enhanced. The measured near-field amplitude is roughly proportional to the electrical field amplitude ($|E_z|$) underneath the tip. Therefore, one expects to observe bright fringes in the case of constructive interference. Due to the limited propagation length of SPPs ($< 1 \mu\text{m}$), we can normally see 1–3 bright fringes. A more detailed introduction to the fringe-formation mechanism can be found in the literature [14,15].

APPENDIX D: MODELING OF THE FRINGE PROFILES

To extract the plasmonic parameters of TLG, we adopt the numerical model from previous work [14]. In this model, we compute quantitatively the SSNOM signals of TLG by considering propagative SPPs. More specifically, the SSNOM tip is approximated as a conducting spheroid, which is a common approach in SSNOM modeling. The SSNOM signal is approximately proportional to the electrical field (E_z) underneath the tip as well as the total dipole moment (p_z) of the tip. TLG is modeled as a plasmonic medium with a complex plasmon wavevector, $q_p = q_1 + iq_2$. The plasmon wavelength, λ_p , equals $2\pi/q_1$, and the plasmon-damping rate is $\gamma_p = q_2/q_1$. In addition, we also consider signal modulation and demodulation due to tip tapping in the modeling.

APPENDIX E: PLASMON-DAMPING RATE OF TLG

We discuss mainly the plasmon wavelength, λ_p , in the main text. In Fig. 8, we plot the extracted plasmon-damping rate, γ_p , of both ABA TLG and ABC TLG. We find that γ_p of ABA TLG and ABC TLG are comparable to each other, and both increase systematically with decreasing carrier density (i.e., as $V_g - V_{CN}$ approaches 0 V). The larger γ_p at smaller doping is possibly due to Landau damping [16], where plasmons decay into electron-hole pairs via interband transitions. In addition, a high carrier density can effectively screen the charged impurities inside the sample and the substrate, so carriers experience less scattering at higher doping.

APPENDIX F: TIGHT-BINDING MODEL AND KUBO FORMULA

To calculate the electronic structures of TLG, we use the tight-binding method. The tight-binding Hamiltonians for ABA TLG and ABC TLG [23,24] are

$$H_{\text{ABA}} = \begin{bmatrix} 0 & \gamma_0 f & \gamma_1 & -\gamma_4 f^* & \frac{\gamma_5}{2} & 0 \\ \gamma_0 f^* & 0 & -\gamma_4 f^* & \gamma_3 f & 0 & \frac{\gamma_2}{2} \\ \gamma_1 & -\gamma_4 f & 0 & \gamma_0 f^* & \gamma_1 & -\gamma_4 f \\ -\gamma_4 f & \gamma_3 f^* & \gamma_0 f & 0 & -\gamma_4 f & \gamma_3 f^* \\ \frac{\gamma_5}{2} & 0 & \gamma_1 & -\gamma_4 f^* & 0 & \gamma_0 f \\ 0 & \frac{\gamma_2}{2} & -\gamma_4 f^* & \gamma_0 f^* & \gamma_0 f(k)^* & 0 \end{bmatrix},$$

$$H_{\text{ABC}} = \begin{bmatrix} 0 & \gamma_0 f & \gamma_1 & -\gamma_4 f^* & 0 & 0 \\ \gamma_0 f^* & 0 & -\gamma_4 f^* & \gamma_3 f & 0 & \frac{\gamma_2}{2} \\ \gamma_0 & -\gamma_4 f & 0 & \gamma_0 f^* & -\gamma_4 f^* & -\gamma_3 f \\ -\gamma_4 f & \gamma_3 f & \gamma_0 f & 0 & -\gamma_1 & -\gamma_4 f^* \\ 0 & 0 & -\gamma_4 f & -\gamma_1 & 0 & \gamma_0 f^* \\ 0 & \frac{\gamma_2}{2} & -\gamma_3 f^* & \gamma_4 f & \gamma_0 f & 0 \end{bmatrix}.$$

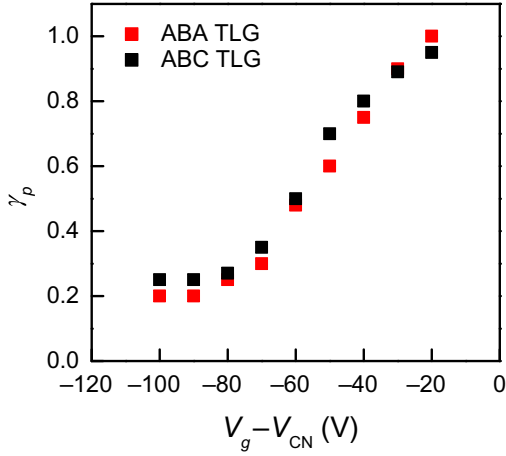


FIG. 8. (a) Plasmon-damping rate, γ_p , extracted by fitting the plasmon fringe profiles in Fig. 3.

Here, the rows and columns follow the order of $A1$, $B1$, $A2$, $B2$, $A3$, and $B3$. Each matrix-element term represents the overlapping of two different atoms. The parameters γ_0 , γ_1 , γ_2 , γ_3 , γ_4 , and γ_5 are Slonczewski-Weiss-McClure (SWMcC) parameters. The parameters used in our calculations are adopted from previous reports in the literature [32,40] and are summarized in Table I. The function f is

$$f(k) = 1 + 2 \cos \frac{k_x a_0}{2} \exp \left(-i \frac{\sqrt{3} k_y a_0}{2} \right),$$

where $a_0 = 2.46 \text{ \AA}$ is the in-plane-basis vector length.

The calculated band structures of ABA TLG and ABC TLG are plotted in Figs. 1(b) and 1(c). Based on the band structures, we calculate the Drude conductivities of ABA

TABLE I. The SWMcC parameters.

Parameter	γ_0	γ_1	γ_2	γ_3	γ_4	γ_5
Value (eV)	3.12	0.377	-0.0206	0.29	0.12	0.025

TLG and ABC TLG using the Kubo formula:

$$\sigma(\omega) = \frac{e^2}{2\pi^2 \hbar} \sum_i \int d^2 k \left| \left\langle k, i \left| \frac{\partial H}{\partial k_x} \right| k, i \right\rangle \right|^2 \times \frac{-\partial f(E_i)}{\partial E} \frac{i}{\hbar \omega + i\gamma_D},$$

where E_i is the band energy at the i th electron band, e is the electron charge, \hbar is the reduced Plank constant, and $\gamma_D = 0.01 \text{ eV}$ is the carrier-scattering energy,

$$f(E) = 1/(1 + e^{(E-E_F/k_B T)}).$$

After we obtain the Drude conductivity of TLG, we then calculate the plasmon wavelength, λ_p , using Eq. (1). The final results of λ_p versus gate voltages are plotted in Fig. 4(a) (solid curves).

- [1] V. Ryzhii, A. Satou, and T. Otsuji, Plasma waves in two-dimensional electron-hole system in gated graphene heterostructures, *J. Appl. Phys.* **101**, 024509 (2007).
- [2] M. Jablan, H. Buljan, and M. Soljačić, Plasmonics in graphene at infrared frequencies, *Phys. Rev. B* **80**, 245435 (2009).
- [3] F. H. L. Koppens, D. E. Chang, and F. Javier García de Abajo, Graphene plasmonics: A platform for strong light-matter interactions, *Nano Lett.* **11**, 3370 (2011).
- [4] A. N. Grigorenko, M. Polini, and K. S. Novoselov, Graphene plasmonics, *Nat. Photonics* **6**, 749 (2012).

- [5] Q. Bao and K. P. Loh, Graphene photonics, plasmonics, and broadband optoelectronic devices, *ACS Nano* **6**, 3677 (2012).
- [6] T. Low and P. Avouris, Graphene plasmonics for terahertz to mid-infrared applications, *ACS Nano* **8**, 1086 (2014).
- [7] D. N. Basov, M. M. Fogler, and F. J. García de Abajo, Polaritons in van der Waals materials, *Science* **354**, 195 (2016).
- [8] T. Low, A. Chaves, J. D. Caldwell, A. Kumar, N. X. Fang, P. Avouris, T. F. Heinz, F. Guinea, L. Martin-Moreno, and F. Koppens, Polaritons in layered two-dimensional materials, *Nat. Mater.* **16**, 182 (2017).
- [9] L. Ju, B. Geng, J. Horng, C. Girit, M. Martin, Z. Hao, H. A. Bechtel, X. Liang, A. Zettl, and Y. R. Shen, *et al.*, Graphene plasmonics for tunable terahertz metamaterials, *Nat. Nanotechnol.* **6**, 630 (2011).
- [10] Z. Fei, G. O. Andreev, W. Bao, L. M. Zhang, A. S. McLeod, C. Wang, M. K. Stewart, Z. Zhao, G. Dominguez, and M. Thiemens, *et al.*, Infrared nanoscopy of Dirac plasmons at the graphene-SiO₂ interface, *Nano Lett.* **11**, 4701 (2011).
- [11] V. W. Brar, M. S. Jang, M. Sherrott, J. J. Lopez, and H. Atwater, Highly confined tunable mid-infrared plasmonics in graphene nanoresonators, *Nano Lett.* **13**, 2541 (2013).
- [12] Z. Fang, S. Thongrattanasiri, A. Schlather, Z. Liu, L. Ma, Y. Wang, P. Ajayan, P. Nordlander, N. J. Halas, and F. J. G. de Abajo, Gated tunability and hybridization of localized plasmons in nanostructured graphene, *ACS Nano* **7**, 2388 (2013).
- [13] W. Gao, G. Shi, Z. Jin, J. Shu, Q. Zhang, R. Vajtai, P. M. Ajayan, J. Kono, and Q. Xu, Excitation and active control of propagating surface plasmon polaritons in graphene, *Nano Lett.* **13**, 3698 (2013).
- [14] Z. Fei, A. S. Rodin, G. O. Andreev, W. Bao, A. S. McLeod, M. Wagner, L. M. Zhang, Z. Zhao, M. Thiemens, and G. Dominguez, *et al.*, Gate-tuning of graphene plasmons revealed by infrared nano-imaging, *Nature* **487**, 82 (2012).
- [15] J. Chen, M. Badioli, P. Alonso-González, S. Thongrattanasiri, F. Huth, J. Osmond, M. Spasenović, A. Centeno, A. Pesquera, and P. Godignon, *et al.*, Optical nano-imaging of gate-tunable graphene plasmons, *Nature* **487**, 77 (2012).
- [16] H. Yan, T. Low, W. Zhu, Y. Wu, M. Freitag, X. Li, F. Guinea, P. Avouris, and F. Xia, Damping pathways of mid-infrared plasmons in graphene nanostructures, *Nat. Photonics* **7**, 394 (2013).
- [17] A. Woessner, M. B. Lundberg, Y. Gao, A. Principi, P. Alonso-González, M. Carrega, K. Watanabe, T. Taniguchi, G. Vignale, and M. Polini, *et al.*, Highly confined low-loss plasmons in graphene-boron nitride heterostructures, *Nat. Mater.* **14**, 421 (2015).
- [18] G. X. Ni, A. S. McLeod, Z. Sun, L. Wang, L. Xiong, K. W. Post, S. S. Sunku, B.-Y. Jiang, J. Hone, and C. R. Dean, *et al.*, Fundamental limits to graphene plasmonics, *Nature* **557**, 530 (2018).
- [19] Z. Fei, E. G. Iwinski, G. X. Ni, L. M. Zhang, W. Bao, A. S. Rodin, Y. Lee, M. Wagner, M. K. Liu, and S. Dai, *et al.*, Tunneling plasmonics in bilayer graphene, *Nano Lett.* **15**, 4973 (2015).
- [20] H. Yan, T. Low, F. Guinea, F. Xia, and P. Avouris, Tunable phonon-induced transparency in bilayer graphene nanoribbons, *Nano Lett.* **14**, 4581 (2014).
- [21] L. Jiang, Z. Shi, B. Zeng, S. Wang, J.-H. Kang, T. Joshi, C. Jin, L. Ju, J. Kim, and T. Lyu, *et al.*, Soliton-dependent plasmon reflection at bilayer graphene domain walls, *Nat. Mater.* **15**, 840 (2016).
- [22] F. Hu, S. R. Das, Y. Luan, T.-F. Chung, Y. P. Chen, and Z. Fei, Real-Space Imaging of the Tailored Plasmons in Twisted Bilayer Graphene, *Phys. Rev. Lett.* **119**, 247402 (2017).
- [23] B. Partoens and F. M. Peeters, From graphene to graphite: Electronic structure around the K point, *Phys. Rev. B* **74**, 075404 (2006).
- [24] A. A. Avetisyan, B. Partoens, and F. M. Peeters, Electric-field control of the band gap and Fermi energy in graphene multilayers by top and back gates, *Phys. Rev. B* **80**, 195401 (2009).
- [25] M. F. Craciun, S. Russo, M. Yamamoto, J. B. Oostinga, A. F. Morpurgo, and S. Tarucha, Trilayer graphene is a semimetal with a gate-tunable band overlap, *Nat. Nanotechnol.* **4**, 383 (2009).
- [26] W. Bao, L. Jing, J. Velasco Jr, Y. Lee, G. Liu, D. Tran, B. Standley, M. Aykol, S. B. Cronin, and D. Smirnov, *et al.*, Stacking-dependent band gap and quantum transport in trilayer graphene, *Nat. Phys.* **7**, 948 (2011).
- [27] S. H. Jhang, M. F. Craciun, S. Schmidmeier, S. Tokumitsu, S. Russo, M. Yamamoto, Y. Skourski, J. Wosnitzer, S. Tarucha, and J. Eroms, *et al.*, Stacking-order dependent transport properties of trilayer graphene, *Phys. Rev. B* **84**, 161408(R) (2011).
- [28] T. Taychatanapat, K. Watanabe, T. Taniguchi, and P. Jarillo-Herrero, Quantum Hall effect and Landau-level crossing of Dirac fermions in trilayer graphene, *Nat. Phys.* **7**, 621 (2011).
- [29] L. Zhang, Y. Zhang, J. Camacho, M. Khodas, and I. Zaluznyak, The experimental observation of quantum Hall effect of $l=3$ chiral quasiparticles in trilayer graphene, *Nat. Phys.* **7**, 9530957 (2011).
- [30] A. Kumar, W. Escoffier, J. M. Poumirol, C. Faugeras, D. P. Arovas, M. M. Fogler, F. Guinea, S. Roche, and M. Goiran, Integer Quantum Hall Effect in Trilayer Graphene, *Phys. Rev. Lett.* **107**, 126806 (2011).
- [31] S. Yuan, R. Roldán, and M. I. Katsnelson, Landau level spectrum of ABA- and ABC-stacked trilayer graphene, *Phys. Rev. B* **84**, 125455 (2011).
- [32] C. H. Lui, Z. Li, M. F. Mak, E. Cappelluti, and T. F. Heinz, Observation of an electrically tunable band gap in trilayer graphene, *Nat. Phys.* **7**, 944 (2011).
- [33] C. Cong, T. Yu, K. Sato, J. Shang, R. Saito, G. F. Dresselhaus, and M. S. Dresselhaus, Raman characterization of ABA- and ABC-stacked trilayer graphene, *ACS Nano* **5**, 8760 (2011).
- [34] D.-S. Kim, H. Kwon, A. Y. Nikitin, S. Ahn, L. Martin-Moreno, F. J. García-Vidal, S. Ryu, H. Min, and Z. H. Kim, Stacking structures of few-layer graphene revealed by phase-sensitive infrared nanoscopy, *ACS Nano* **9**, 6765 (2015).
- [35] L. Jiang, S. Wang, Z. Shi, C. Jin, M. L. B. Utama, S. Zhao, Y.-R. Shen, H.-J. Gao, G. Zhang, and F. Wang, Manipulation of domain-wall solitons in bi- and trilayer graphene, *Nat. Nanotechnol.* **13**, 204 (2018).

- [36] H. Li, I. B. Utama, S. Wang, W. Zhao, S. Zhao, X. Xiao, Y. Jiang, L. Jiang, T. Taniguchi, and K. Watanabe, *et al.*, Global control of stacking-order phase transition by doping and electric field in few-layer graphene, *Nano Lett.* **5**, 3106 (2020).
- [37] Z. Gao, S. Wang, J. Berry, Q. Zhang, J. Gebhardt, W. M. Parkin, J. Avila, H. Yi, C. Chen, and S. Hurtado-Parra, *et al.*, Large-area epitaxial growth of curvature-stabilized ABC trilayer graphene, *Nat. Commun.* **11**, 546 (2020).
- [38] J. Zhang, J. Han, G. Peng, X. Yang, X. Yuan, Y. Li, J. Chen, W. Xu, K. Liu, and Z. Zhu, *et al.*, Light-induced irreversible structural phase transition in trilayer graphene, *Light Sci. Appl.* **9**, 174 (2020).
- [39] J. Qian, Y. Luan, M. Kim, K.-M. Ho, Y. Shi, C.-Z. Wang, Y. Li, and Z. Fei, Nonequilibrium phonon tuning and mapping in few-layer graphene with infrared nanoscopy, *Phys Rev. B* **103**, L201407 (2021).
- [40] N. Ubrig, P. Blake, D. van der Marel, and A. B. Kuzmenko, Infrared spectroscopy of hole doped ABA-stacked trilayer graphene, *Europhys. Lett.* **100**, 58003 (2012).
- [41] T. Latychevskaia, S.-K. Son, Y. Yang, D. Chancellor, M. Brown, S. Ozdemir, I. Madan, G. Berruto, F. Carbone, and A. Mishchenko, *et al.*, Stacking transition in rhombohedral graphite, *Front. Phys.* **14**, 13608 (2019).
- [42] M. Yankowitz, J. I.-J. Wang, A. G. Birdwell, Y.-A. Chen, K. Watanabe, T. Taniguchi, P. Jacquod, P. San-Jose, P. Jaribbo-Herrero, and B. J. LeRoy, Electric field control of soliton motion and stacking in trilayer graphene, *Nat. Mater.* **13**, 786 (2014).
- [43] W. Zhang, J. Yan, C.-H. Chen, L. Lei, J.-L. Kuo, Z. Shen, and L.-J. Li, Molecular adsorption induces the transformation of rhombohedral- to Bernal-stacking order in trilayer graphene, *Nat. Commun.* **4**, 2074 (2013).
- [44] N. Delikoukos, D. Tasis, A. Michail, J. Parthenios, E. N. Koukaras, and K. Papagelis, Doping-induced stacking transition in trilayer graphene: Implications for layer stacking manipulation, *ACS Appl. Nano Mater.* **3**, 11861 (2020).